Dynamic phantom with two stage-driven absorbers for mimicking hemoglobin changes in superficial and deep tissues

Tsukasa Funane
Hirokazu Atsumori
Masashi Kiguchi
Yukari Tanikawa
Eiji Okada

Dynamic phantom with two stage-driven absorbers for mimicking hemoglobin changes in superficial and deep tissues

Tsukasa Funane,a,c Hirokazu Atsumori,a Masashi Kiguchi,a Yukari Tanikawa,b and Eiji Okadac
aHitachi Ltd., Central Research Laboratory, Hatoyama, Saitama 350-0395, Japan
bNational Institute of Advanced Industrial Science and Technology, Ibaraki 305-8564, Japan
cKeio University, Department of Electronics and Electrical Engineering, Yokohama 223-8522, Japan

Abstract. In near-infrared spectroscopy (NIRS) for monitoring brain activity and cerebral functional connectivity, the effect of superficial tissue on NIRS signals needs to be considered. Although some methods for determining the effect of scalp and brain have been proposed, direct validation of the methods has been difficult because the actual absorption changes cannot be known. In response to this problem, we developed a dynamic phantom that mimics hemoglobin changes in superficial and deep tissues, thus allowing us to experimentally validate the methods. Two absorber layers are independently driven with two one-axis automatic stages. We can use the phantom to design any type of waveform (e.g., brain activity or systemic fluctuation) of absorption change, which can then be reproducibly measured. To determine the effectiveness of the phantom, we used it for a multiple source-detector distance measurement. We also investigated the performance of a subtraction method with a short-distance regressor. The most accurate lower-layer change was obtained when a shortest-distance channel was used. Furthermore, when an independent component analysis was applied to the same data, the extracted components were in good agreement with the actual signals. These results demonstrate that the proposed phantom can be used for evaluating methods of discriminating the effects of superficial tissue. © *2012 Society of Photo-Optical Instrumentation Engineers (SPIE).* [DOI: 10.1117/1.JBO.17.4.047001]

1 Introduction

The measurement of hemoglobin (Hb) changes in biological tissue by near-infrared spectroscopy (NIRS) has been used for brain-function monitoring systems[1–4] such as optical topography[5–8] in which the image of hemodynamic responses related to neural activities are measured noninvasively. This technique has been widely used in research related to language[9] and infants[10,11] as well as for clinical purposes[12,13] due to its advantageous features, which include noninvasiveness,[14,15] low constraint, and portability.[16–18]

In this technique, the scalp is irradiated with near-infrared light, and the light that is propagated in and scattered from the tissue is detected at another position. Therefore, the light attenuation is influenced by the blood volume in superficial tissue. The NIR light propagates in superficial tissue even when a deep region of the tissue is of interest, and accordingly, if they are not negligible, the effects of superficial tissue on the NIRS signal should be taken into account.[19–22] Previous studies have shown that in brain measurements, the thickness of the scalp and the skull has an interference effect on the NIRS signal.[23,24] Several methods have been proposed to eliminate the effect of scalp-blood flow, systemic signal, and biological fluctuation, including using principal component analysis (PCA),[25,26] independent component analysis (ICA),[27,28] and an inter-channel subtraction method with multiple-distance optodes.[29–38] The

final method is often used in conjunction with static linear-regression,[29–31] adaptive filtering,[35–37] and Kalman filtering.[38]

ICA and PCA are the analytical methods that use continuous waveform or time-course data (patterns), and therefore it is difficult to evaluate them with a static or two-state (on or off) dynamic phantom. Instead, such signal discrimination methods are usually evaluated with simulations.[32,33,35,37] In terms of application to human measurements, the validity has been evaluated by other biological signals measured with laser Doppler flowmetry,[27] or by synchronization with task timing,[28] and/or simulated hemodynamic response[31,38] because the correct signal from the cerebral tissue cannot be known during the actual measuring.

With a tissue-mimicking phantom,[39] the correct absorption change is known because the optical properties and shape of the phantom material can be reproducibly realized[40] and can be validated with a Monte Carlo simulation based on the same model as the phantom. Clearly, using the phantom is effective for evaluating methods that eliminate and discriminate the effect of superficial tissue from that of deep tissue in NIRS signals. To evaluate such methods directly and quantitatively, a dynamic phantom with a high reproducibility and ability to make any waveform (e.g., designed time course data) of absorption is necessary. Waveforms have several properties, including frequency characteristics and correlation with other waveforms. If we use a waveform that has been created by a phantom, we can investigate the influence of waveform properties on the performance of the discriminating methods.

Address all correspondence to:Tsukasa Funane, Hitachi, Ltd., Central Research Laboratory, Hatoyama, Saitama 350-0395, Japan. Tel: +81-49-296-6111; Fax: +81-49-296-5999; E-mail: tsukasa.funane.sb@hitachi.com.

Some dynamic phantoms with liquid perfusion have previously been reported.[41–43] The response time of these phantoms is relatively slow, which makes it difficult to force the waveform of absorption to change in a practical period of time. Therefore, the reproducibility of the fast absorption change is hard to guarantee. The use of a dynamic phantom with an embedded liquid crystal has been proposed,[44] in which the absorption at each pixel is electrically controlled. However, each pixel can be only on- or off-state (in other words, two-state control), meaning that a small absorption change in a superficial layer of the phantom cannot be achieved with this phantom.

The aim of the present study is to develop a methodology that can directly evaluate analytical methods for discriminating surface-layer effect. A tissue-simulating dynamic phantom with two absorption layers ("upper" and "lower") was developed. This type of phantom only creates macroscopic absorption changes in tissue and cannot mimic the microscopic spatial variability and mechanism of hemodynamics due to vasculature. It is important to understand the limitation of the applicability of the phantom and that the experimental results of the phantom cannot be easily generalized. However, the phantom is very useful and indeed essential for industrial applications such as the performance testing of NIRS instruments. Its key feature is that the effective absorption coefficient can be adjusted by changing the position of the absorber. The waveform of absorption change can be reproducibly simulated by two one-axis stage-driven absorbers within a very short period of time. Using a multidistance NIRS system,[45] we measured the optical density change of the phantom at multiple source-detector (S-D) distances and investigated the performance of a subtraction method with a short-distance regressor. In addition, when the absorption coefficients of two layers were changed, we extracted the signal of each layer by ICA and investigated the dependence of the weight of each component on the S-D distance.

2 Design of Dynamic Phantom

2.1 Material and Structure of Phantom

We used reports by Fukui et al.[46] and Wang et al.[47] to set the absorption coefficient (μ_a) and reduced scattering coefficient (μ_s') values of the scalp and skull and the gray matter of a human adult head to the range of 0.012 to 0.036 and 0.73 to 2.3 mm^{-1}, respectively. In this study, the μ_a and μ_s' values of the two layers of absorber were chosen from around this range. A white polyoxymethylene (POM) was used as the base material of the phantom because it has a comparable μ_s' value (0.9 mm^{-1}) to biological tissue and is commercially available and easily worked, although it does not absorb light very

much ($\mu_a = 0.002$ mm^{-1}). Three absorber materials with μ_a values of 0.01, 0.02, and 0.03 mm^{-1} were thus prepared. The μ_s' value of the absorbers was 0.9 mm^{-1} to match that of the POM. The absorbers were made by mixing an epoxy resin (MY753, Aeropia Chemical Supplies) and a hardener (XD716, Aeropia Chemical Supplies) at a 3∶1 weight ratio.[48] An infrared dye, Projet 830 (Avecia Ltd.), and titanium dioxide (SuperWhite, Alec Tiranti Ltd.) were mixed into the absorber materials to control the absorption coefficient and the reduced scattering coefficient of the absorbers, respectively.

Using these materials, a phantom with two absorber layers (upper and lower) in low-absorption and high-scattering base material was developed. The phantom size was 100×120 (horizontal) $\times 60$ (vertical) mm. The absorbers ($75 \times 60 \times 5$ mm) were held by absorber-holing frames (made of white POM) and were inserted into two cavities ($100 \times 70 \times 5$ mm) at depths of 2 to 7 mm and 12 to 17 mm. The hexagon socket set screw was used to attach the absorber to the absorber-holding frames. These frames, along with an overall view of the developed dynamic phantom, are shown in Fig. 1. One absorber-holding frame was attached to each automatic stage with an aluminum spacer between the aluminum frame and the stage.

In our phantom model, to uphold the assumption that an absorber's position change in a layer region is equivalent to a homogeneous μ_a change in the corresponding layer region, the thickness of each absorber (and absorber-holding frame) should be sufficiently larger than photon-transport length scales (approx. $1/\mu_s'$). The depth (12 mm) and thickness (5 mm) of the lower layer was chosen from around the values of reported scalp-cortex distance (12 to 18 mm) and thickness of gray matter (4 mm).[49,50] The thickness of the upper layer (5 mm) was also chosen from the reported value of scalp thickness (3.0 to 7.1 mm).[49,50] The upper-layer simulating scalp should be as shallow as possible, but we put a 2-mm-thick superficial layer (scatterer) over the upper layer to strengthen the structure of the phantom. In this way, we determined the depth and thickness of each layer not simply based on anatomical considerations but also on the design of a phantom for industrial purposes.

2.2 Driving Mechanism of Absorbers

To dynamically change the position of absorbers in the phantom, two layers of absorbers were held in place by absorber-holding frames using two one-axis automatic stages (SGSP20-85, Sigma Koki Co., Ltd.). The stage and absorber-holding frame was connected to an aluminum frame. The two stages were controlled by a PC that transmitted commands to the stage controller via RS232C. Each absorber-holding frame was thus independently controlled by a corresponding one-axis automatic stage.
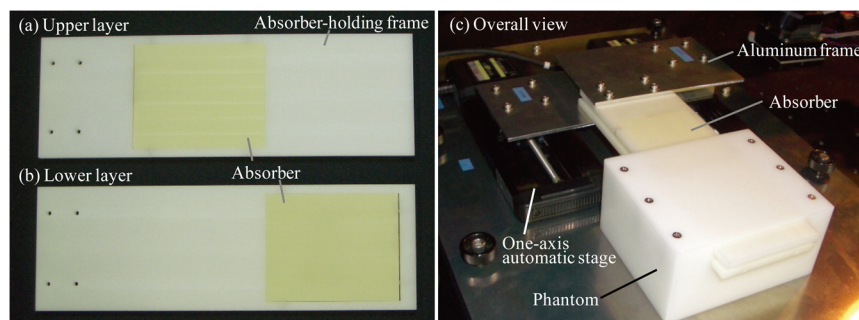
Fig. 1 Photos of the developed phantom. (a) Upper layer and (b) lower layer of absorber-holding frame. (c) Overall view of dynamic phantom.
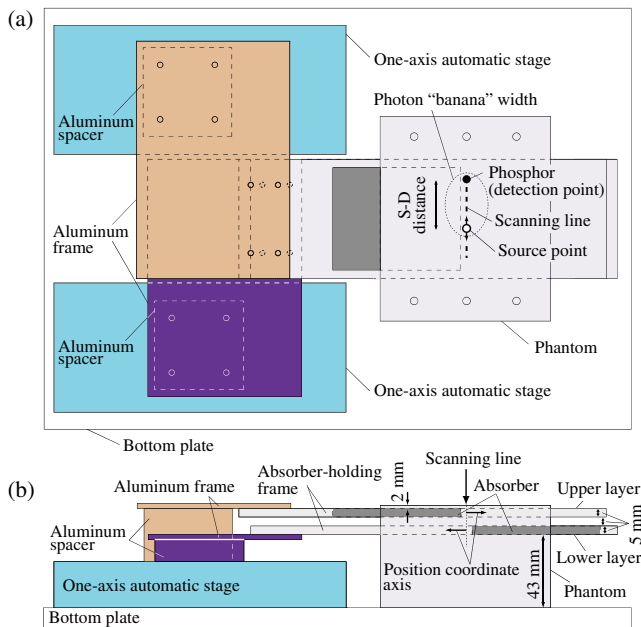
Fig. 2 Structure of phantom and driving mechanism of absorbers. (a) Top view. (b) Front view. Each absorber-holding frame is independently controlled by a corresponding one-axis automatic stage.

The automatic stages and the phantom were attached to an aluminum bottom plate. The structure of the phantom and the driving mechanism is shown in Fig. 2. Figure 2(a) shows a top view of the phantom showing one source point, the phosphor detector point, an outline of the "banana" width of the photon spatial distribution, and one of the absorber slabs (superimposed). Figure 2(b) shows a front view of the phantom. Each absorber-holding frame is independently controlled by a corresponding one-axis automatic stage.

Two absorbers were placed on the opposite side from the center line (scanning line) so that sensitivity to the absorption change of each layer would not be much influenced by the absorption change of another layer. The opposite-side placement minimizes the number of photons that propagates in both absorbers, whereas same-side placement maximizes it. Therefore, the opposite-side placement of absorbers minimizes any interaction effects between two absorbers that could lead to nonlinearity between the position and the ΔOD.

The target position was converted to the stroke in stage coordinate value and sent as a command from the PC to the stage controller. The origin and positive or negative direction of the position coordinate axes were set so that the partial optical path length in the absorber was increased (i.e., the optical density was increased) when the stage position was positive in the defined coordinate axis (hereafter, "x" used for the place coordinates for both layers). Therefore, the directions of the position coordinates for the upper and lower layers were set to be opposite. Optical density change (i.e., effective $\Delta\mu_a$) was controlled by the partial effective path length in absorbers that was determined by the stage-position change (Δx), not by the $\Delta\mu_a$ of the absorber.

3 Measurement System

To test the dynamic phantom developed in this study, we used a multidistance NIRS system with a noncontact light source (an 808-nm laser diode) and detector that effectively measures the optical density of the biological tissue at multiple S-D
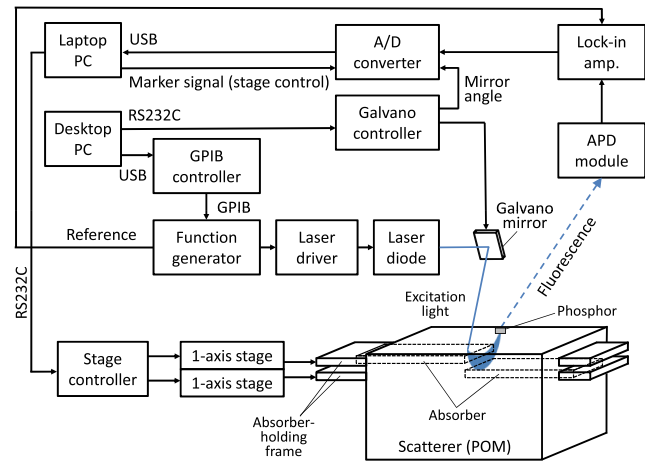
Fig. 3 Block diagram of multidistance NIRS system and stage controller for phantom. Two one-axis stages are independently driven by a stage controller that is commanded by a laptop PC through RS232C.

separations.[45] To make it possible to measure the absorption change of tissue with a noncontact light emitter and detector, the wavelength of the tissue-propagated light was converted by a near-infrared phosphor on the surface of tissue, and the excitation light was cut by optical filters; consequently, only fluorescence was detected and discriminated with lock-in detection, whereas any backscattered stray light was suppressed.[51,52] Phosphor $[Li(Nd_{0.9}Yb_{0.1})P_4O_{12}]$, which was enclosed and bonded in a cell consisting of an aluminum ring and an Indium phosphide (InP) wafer, was placed on a fixed detection focal point.

A block diagram of the multidistance NIRS system and stage controller for the phantom are shown in Fig. 3. The laser diode was driven by a laser driver (ALP-7033CB, Asahi Data Systems Co., Ltd.) that receives the analog signal of a function generator (model 1930A, NF Corporation). The frequency of intensity modulation was set to 3.3 kHz. The function generator was controlled via a general purpose interface bus (GPIB) controller (GPIB-USB-HS, National Instruments Corporation) with a desktop PC, which meant we could adjust the irradiation power of the laser diode in accordance with the S-D distance. A galvano scanner (controller: GC-201; motor: GM-1010; Canon Inc.) was controlled via RS232C with the desktop PC.

The fluorescence emitted from the phosphor and caught by the advanced performance detectors (APD) is amplified by a transimpedance amplifier in an APD module, and after that the amplified fluorescence signal is detected by a lock-in amplifier (model 5207, EG&G), the output of which is converted to a digital signal by an analog-digital converter (NR-2000, Keyence Corporation) and saved in a laptop PC via USB. An analog marker signal was input into the analog-digital converter from the laptop PC.

The galvano scanner was set to irradiate 10 points on the phantom surface, where S-D distances were set to 5.5 to 41.5 mm with a 4-mm interval for each. The duration of the measurement of each point was 1 s including switching time of the measurement point and irradiation power.

4 Calibration of Dynamic Phantom

4.1 Calibration Method

A calibration curve of the relationship between the stage position and changes in optical density (ΔOD) is necessary in order

to use the phantom for NIRS measurement. To calibrate the phantom, its ΔOD was measured as the inserted absorber at either of the upper or lower layers driven by a one-axis automatic stage. The layer that is not driven is replaced by base material (white POM) by setting the stage positions to $x = -37$ and -43 mm for the upper and lower layers, respectively. ΔOD was calculated by

$$\Delta OD = -\ln \frac{I}{I_0}, \quad (1)$$

where I_0 represents the baseline intensity of detected light that is obtained when the stage position is $x = -30$ mm. I represents the intensity of detected light at each stage position. The absorption coefficients of the upper and lower layers are 0.01 and 0.03 mm^{-1}, respectively.

4.2 Relationship Between Stage Position and ΔOD

To ensure a linear relationship between the stage-position change (Δx) and ΔOD for both layers, and to minimize the interaction effect between two absorber layers, the absorption coefficient of the upper layer should be smaller. Furthermore, in terms of phantom design, to make the ΔOD values at a typical S-D distance (for example, 29.5 mm) caused by the movements of two absorber layers as equal as possible, the absorption coefficient of the lower layer should be higher than that of the upper layer. Among all combinations of μ_a values, we selected 0.01 and 0.03 mm^{-1} for the upper and lower layers, respectively.
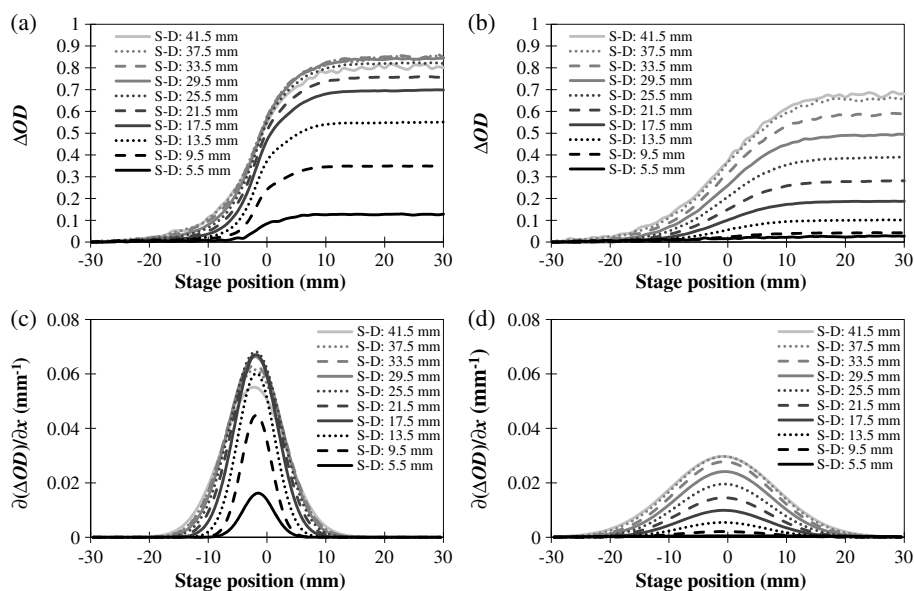
The relationship between stage position (the coordinates of which are defined in Sec. 2.2) and ΔOD for 10 different S-D distances is shown in Fig. 4(a) and 4(b). Figure 4(a) describes ΔOD changes as only the upper layer being driven (μ_a of absorber: 0.01 mm^{-1}), and Fig. 4(b) describes ΔOD changes as only the lower layer being driven (μ_a of absorber: 0.03 mm^{-1}). In Fig. 4(a), the inflection point of ΔOD is deviated to the minus side because the photon distribution is changed due to the movement of the upper-layer absorber.

In contrast, the deviation from the center line of the inflection point of ΔOD for the lower layer is relatively smaller than that for the upper layer because the ratio of partial effective path length in the lower absorber to total path length is smaller than that in the upper absorber, and the influence of stage position on the photon distribution in the phantom is relatively small.

Moreover, in both conditions (a) and (b), the initial rise of ΔOD while increasing the stage position from $x = -30$ mm is earlier for the longer S-D distance because the spatial distribution of photons in the phantom is larger for the longer S-D distance probe, and the probe is sensitive to the absorber that is further from the center line ($x = 0$ in the position coordinate).

To quantify the deviation of the inflection point of ΔOD from the center point, we calculated the gradient of ΔOD. The relationship between the stage position and the stage-axial spatial gradient of the ΔOD [$\partial(\Delta OD)/\partial x$] at each S-D distance is shown in Fig. 4(c) and 4(d). Figure 4(c) describes $\partial(\Delta OD)/\partial x$ changes as only the upper layer being driven (μ_a of absorber: 0.01 mm^{-1}) and Fig. 4(d) describes $\partial(\Delta OD)/\partial x$ changes as only the lower layer being driven (μ_a of absorber: 0.03 mm^{-1}). The Gaussian curves fitted to the ΔOD gradient of the measurement data are shown in the figures. The mean stage positions at the maximal ΔOD gradient were $x = -1.9$ mm (upper layer) and $x = -0.7$ mm (lower layer). The mean values and standard deviations of full width at half maximum (FWHM) of the ΔOD gradient were 9.4 ± 2.3mm (upper layer) and 19 ± 1.5mm (lower layer). The minimum FWHM values were 6.0 mm at 9.5-mm S-D distance and 16.8 mm at 13.5-mm S-D distance for the upper and lower layers, respectively. The ΔOD gradient at the 5.5-mm S-D distance was not used to calculate the mean position or FWHM for the lower layer because the ΔOD gradient was almost equal to zero.

To proportionally change the ΔOD by the change of the stage position, the stage should be driven within the range where the spatial slope of ΔOD is constant. When an approximate-linearity of the relationship between changes in stage position and ΔOD was defined as the stage positions where the change in ΔOD gradient is within 10% from the maximum (at the inflection point),

Fig. 4 Calibration results. Relationship between stage position and ΔOD for 10 conditions of S-D distance when (a) only upper layer (μ_a of absorber: 0.01 mm^{-1}) was driven and (b) only lower layer (μ_a of absorber: 0.03 mm^{-1}) was driven. Gradient of ΔOD at each stage position for 10 conditions of S-D distance when (c) only upper layer (μ_a of absorber: 0.01 mm^{-1}) was driven and (d) only lower layer (μ_a of absorber: 0.03 mm^{-1}) was driven.

the calculated ranges were $x = -1.9 \pm 1.8$ and $x = -0.7 \pm 3.6$ mm for the upper and lower layers, respectively. The ranges were calculated by using the mean FWHM values of the ΔOD gradient as representative values. The waveform of ΔOD was approximately the same as that of the stage position when the stages were driven within the range; therefore, the ΔOD change profile can be easily designed. The waveforms of the driving stages used for the following experiments were designed so that the stage positions were all within the above range.

4.3 Comparison with Results by Monte Carlo Simulation

To investigate the consistency between the developed phantom and a simulation model where the same μ_a and μ_s' were assumed, ΔOD measured while each layer region was switched from uniform POM to uniform absorber (ΔOD$_{\text{sw}}$) was compared with the linear-fitted partial effective path length (L_{eff}) of photons calculated by a three-dimensional (3-D) Monte Carlo simulation[53–55] in the following way.

From experiments, ΔOD$_{\text{sw}}$ was obtained by the ΔOD measured at the 30-mm position where each layer region underneath the measurement optodes was switched from uniform POM to uniform absorber, while another layer was uniform POM. Monte Carlo simulation was used to calculate the $L_{\text{eff}}^{\text{upper}}$ and $L_{\text{eff}}^{\text{lower}}$ values by using absorption coefficients $(\mu_a^{\text{upper}}, \mu_a^{\text{lower}}) = (0.01, 0.002)$ and $(0.002, 0.03)$ (mm^{-1}), respectively. When the change in the product of absorption coefficient and partial effective path length is assumed to be equal to ΔOD,[54] ΔOD is expressed as:

$$\Delta\text{OD} = \Delta(\mu_a^{\text{upper}} \times L_{\text{eff}}^{\text{upper}}) + \Delta(\mu_a^{\text{lower}} \times L_{\text{eff}}^{\text{lower}}), \quad (2)$$

where $L_{\text{eff}}^{\text{upper}}$ and $L_{\text{eff}}^{\text{lower}}$ represent partial effective path lengths for the upper and lower layers, respectively. The L_{eff} values at 5-, 10-, 15-, 20-, 25-, 30-, 35-, 40-, and 45-mm S-D distances calculated by Monte Carlo simulation were interpolated to values at 5.5-, 9.5-, 13.5-, 17.5-, 21.5-, 25.5-, 29.5-, 33.5-, 37.5-, and 41.5-mm S-D distances by a spline function. Next, the spline function was fitted to the measured ΔOD$_{\text{sw}}$ by a least-square method and a single scaling factor that provided the best overall fit (which we call "computed ΔOD") to the experimental ΔOD$_{\text{sw}}$ for each layer was obtained. Furthermore, to quantitate the performance of a regression method, we defined and calculated the "ratio of ΔOD($R_{\Delta\text{OD}}$)" between the upper and lower layers, expressed as:

$$R_{\Delta\text{OD}} = \frac{\Delta\text{OD}^{\text{upper}}}{\Delta\text{OD}^{\text{lower}}}, \quad (3)$$

where computed ΔOD values were used.

The data obtained at the longest S-D distance (41.5 mm) was not used for the fitting because of a low signal-to-noise ratio. The obtained scaling factors were 0.010 and 0.023 mm^{-1} for upper- and lower-layer L_{eff}, respectively. The experimental ΔOD$_{\text{sw}}$, the computed ΔOD (linear fit of the simulated L_{eff}) of each layer, and the ratio of ΔOD at each S-D distance are plotted in Fig. 5(a). The goodness of fit between the experimental and computed ΔOD was tested using the chi-square test. Results showed that the validity of the model (spline function from computed L_{eff}), including S-D distance dependency of ΔOD for each layer, was warranted [reduced chi-square: $\chi^2 = 0.0003$ (upper), 0.017 (lower) <1]. According to Eq. (2), when
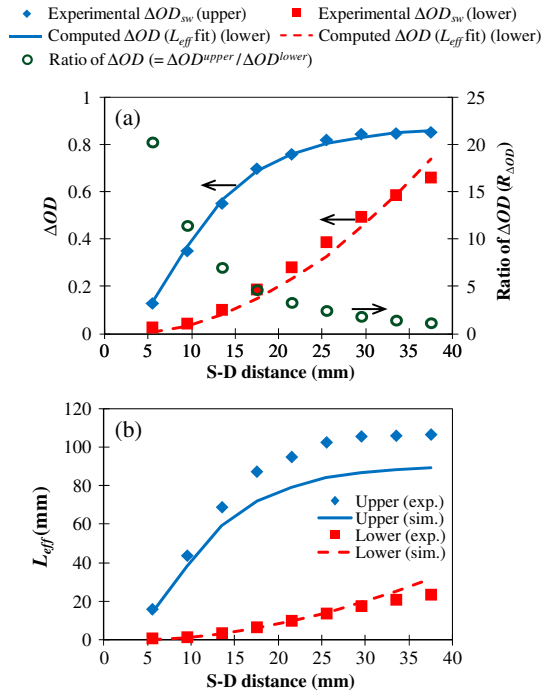
Fig. 5 (a) Experimental ΔOD$_{\text{sw}}$, the computed ΔOD (linear fit of the simulated L_{eff}) of each layer, and the ratio of ΔOD($R_{\Delta\text{OD}}$) at each S-D distance. (b) Experimental (exp.) and simulated (sim.) L_{eff} of upper and lower layers. Experimental L_{eff} was calculated using ΔOD$_{\text{sw}}$ and $\Delta\mu_a$. When ΔOD$_{\text{sw}}$ was measured, absorption coefficients of upper and lower layers were changed from 0.002 to 0.01 mm^{-1} and from 0.002 to 0.03 mm^{-1}, respectively. In the Monte Carlo simulation, absorption coefficients of the upper and lower layers were set to 0.01 and 0.03 mm^{-1}, respectively.

L_{eff} values are constant and the $\Delta\mu_a$ of either the upper or lower layer is equal to zero, the obtained scaling factor should be comparable to $\Delta\mu_a$. The scaling factors for the upper and lower layers are therefore expected to be 0.008 (0.010 to 0.002) and 0.028 (0.030 to 0.002) mm^{-1}, respectively, which are the values of the assumed absorption-coefficient changes. The differences between the scaling factor and acual experimental $\Delta\mu_a$ were 20% and 22%.

The L_{eff} values computed by Monte Carlo simulation and the experimental L_{eff} values ($=\Delta$OD$_{\text{sw}}/\Delta\mu_a$) are shown in Fig. 5(b). Experimental L_{eff} values were calculated using expected $\Delta\mu_a$ values. The differences between the L_{eff} values from the measurement and the simulation were, on average, 19.0% and 9.4% (L_{eff} at a S-D distance of 5.5 mm for the lower layer was not used because the L_{eff} from the simulation was almost equal to zero, so the error was 240%). The difference of the values between experiment and simulation could have been caused by 1. an inaccurate measurement of the absorber's optical properties, 2. the difference between the photon distributions (and subsequent L_{eff} change) under the condition when the lower layer was filled with absorber and the condition when it was not, or 3. measurement noise during the experiments.

5 Evaluation of Multidistance Analytical Methods by Dynamic Phantom

5.1 Synthesis of Waveforms

We used the phantom to evaluate the multidistance analytical methods for discriminating the effects of superficial tissue in
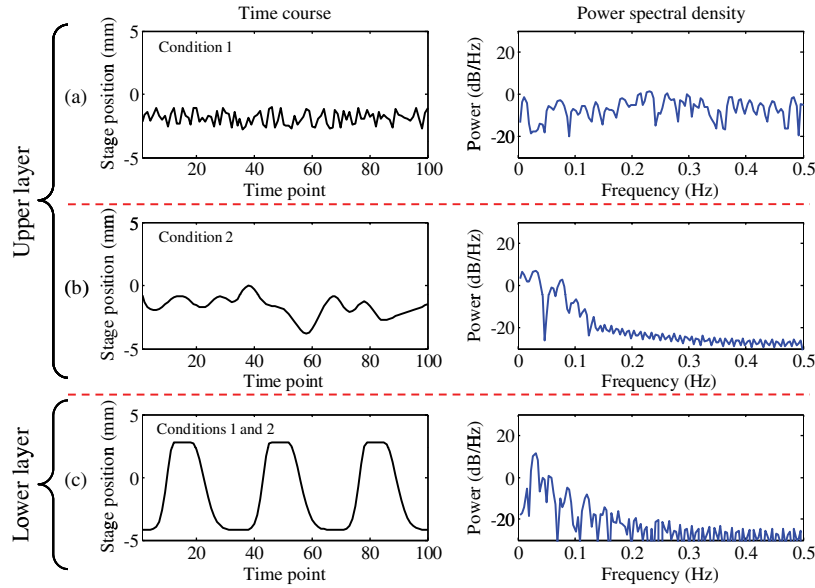
Fig. 6 Time course and power spectrum density (PSD) of stage-position change simulating NIRS signal when one point of time course data was equivalent to 1 sec: (a) white noise, (b) biological fluctuation, and (c) cerebral blood volume (CBV) response evoked by neuronal activation.

the following way. The waveform of the absorption change at each layer can be easily reproduced by controlling the 1-axis stage with digital-base commands. While the upper and lower layers were driven under the following two conditions, ΔOD was measured by the multidistance NIRS system described in Sec. 3. Measurements were also conducted while only one layer was driven under the two conditions.

Under condition 1, the stage position of the upper layer was driven so as to simulate white noise while the stage position of the lower layer was driven so as to simulate a change in cerebral blood volume (CBV)[56] evoked by neural activation. Under condition 2, the stage position of the upper layer was driven so as to simulate a biological fluctuation,[57,58] while the stage position of the lower layer was driven so as to simulate a change in CBV response. All three simulated waveforms could be obtained with the *in vivo* NIRS measurement.

Three types of time-course data, along with the power spectral densities of the stage-position changes, are shown in Fig. 6(a) white noise, 6(b) biological fluctuation, and 6(c) CBV response. The time-course data were normalized to zero-mean and unit-variance data when the power spectrum densities were calculated. Power spectral densities were calculated on the assumption that one point of time-course data is equivalent to 1 sec. At frequencies lower than 0.1 Hz, the waveforms in 6(b) and 6(c) commonly have a lot of power compared to those at higher frequencies. These two waveforms cannot thus be discriminated with frequency filtering. The correlation coefficients between the waveforms in 6(a) and 6(c) and those in 6(b) and 6(c) were 0.015 and −0.190, respectively.

5.2 Extraction of Deep-Layer Signal with Subtraction Method

Using our dynamic phantom, the performance of a subtraction method with short-separation regression,[29–31] which extracts the deep absorption change from a signal that is contaminated by the absorption change of the surface layer, was investigated while both absorbers of the upper and lower layers were independently driven. In the subtraction method, the signal from a short S-D

distance channel was linearly fitted to that from a long-distance channel.[29–31] In the present study, we compare the result from the method with the correct waveform that was obtained while only the lower layer was driven. Performance was defined as the amplitude ratio of the subtraction result to actual lower layer change (target).

When the subtraction method is used, lower-layer signal amplitude at a longer S-D distance (ΔOD$_{\text{SD1}}^{\text{lower}}$) is also subtracted by a lower-layer signal that is included in the shorter S-D distance signal (regressor channel) (ΔOD$_{\text{SD2}}^{\text{lower}}$), where the scaling factor is the ratio of the upper-layer ΔOD of longer S-D distance to shorter S-D distance (ΔOD$_{\text{SD1}}^{\text{upper}}/\Delta$OD$_{\text{SD2}}^{\text{upper}}$) because subtraction is performed so as to eliminate the upper-layer signal. If the performance of the subtraction method is defined as the amplitude ratio (AR) of the subtraction result to only the lower-layer change (target), AR can be expressed as:

$$\text{AR} = \left(\Delta\text{OD}_{\text{SD1}}^{\text{lower}} - \frac{\Delta\text{OD}_{\text{SD1}}^{\text{upper}}}{\Delta\text{OD}_{\text{SD2}}^{\text{upper}}} \times \Delta\text{OD}_{\text{SD2}}^{\text{lower}} \right) / \Delta\text{OD}_{\text{SD1}}^{\text{lower}}$$

$$= 1 - \frac{\Delta\text{OD}_{\text{SD1}}^{\text{upper}}}{\Delta\text{OD}_{\text{SD1}}^{\text{lower}}} \times \frac{\Delta\text{OD}_{\text{SD2}}^{\text{lower}}}{\Delta\text{OD}_{\text{SD2}}^{\text{upper}}}, \tag{4}$$

$$= 1 - \frac{R_{\Delta\text{OD}}^{\text{SD1}}}{R_{\Delta\text{OD}}^{\text{SD2}}}, \tag{5}$$

where each ΔOD value is a representative value under each condition, and SD1 and SD2 are the longer and shorter S-D distances, respectively. Thus the subtraction performance depends not only on the regressor (or shorter) channel but also on the longer channel. Experimental results were used to compare experimental AR and computed AR. The experimental AR values were calculated using the ratio of the mean value of experimental ΔOD over time points where the lower-layer change (target) has a max value (time points: 13 to 18, 46 to 51, 79 to 85). Computed AR were calculated using $R_{\Delta\text{OD}}$, which was obtained by computed ΔOD.
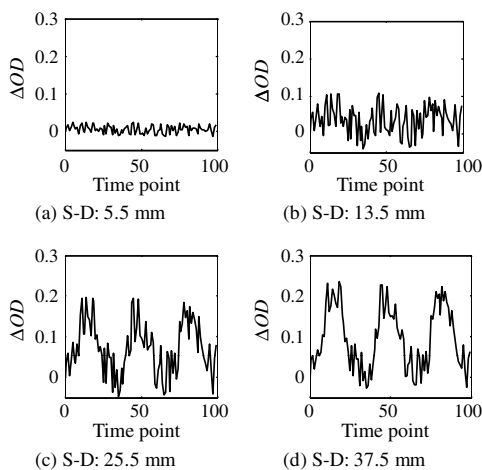
5.3 Results of Performance Evaluation of Subtraction Method

The ΔOD measured at each S-D distance when the upper and lower layers were driven in white-noise and a CBV waveform, respectively (condition 1), is shown in Fig. 7. Mixed signals of white-noise and CBV waveforms were obtained, but almost the same shape of CBV signal can be observed in ΔOD signals at longer S-D distances. The subtraction results with the short-distance regression of ΔOD measured while both layers were driven under condition 1, along with ΔOD that was measured at a long distance while only the lower layer was singly driven (target), are shown in Fig. 8. The noise that is commonly present in ΔOD signals at all S-D distances was eliminated, and a CBV signal of the lower layer was clearly obtained when the shortest S-D distance (5.5 mm) channel was used.
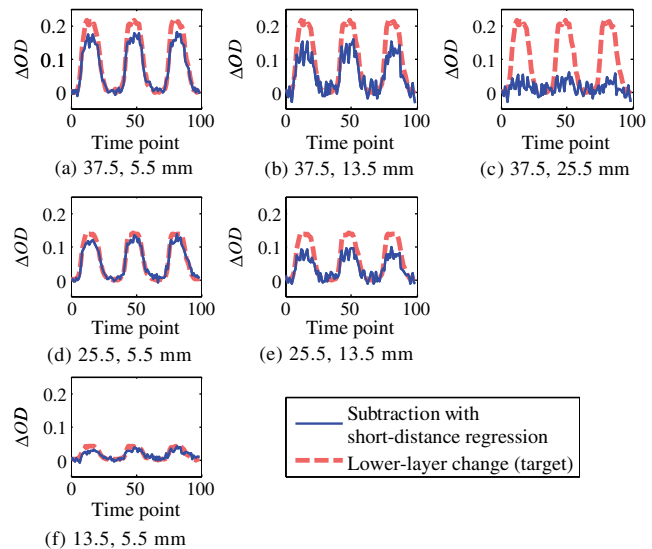
The results under condition 2 are shown in Figs. 9 and 10. As seen in Fig. 10, even if the tendency of the CBV response was not clearly visible from the raw ΔOD signal, the CBV signal at the lower layer was obtained when the shortest S-D distance channel was used. The subtraction method was effective even under the condition that the two waveforms had power in the same frequency range (Fig. 6).

Table 1(a)–(c) shows the performance of the subtraction method defined as the amplitude ratios (AR) of the subtraction result to only the lower-layer change (target) under three conditions: (a) AR from computed ΔOD, (b) experimental AR under condition 1, and (c) experimental AR under condition 2. The mean error and its standard deviation of experimental AR from computed AR was $23 \pm 22\%$, but under four conditions of S-D distance combinations, the errors were less than 10%. For example, when 25.5- and 5.5-mm S-D distances were used under condition 1, the error was only 2.5%. These errors might have been caused by several factors, such as waveform combination or method of calculating AR. We demonstrated that the approximate performance of the subtraction method can be estimated by the computed AR and that a shorter S-D distance is better for a regressor.

A CBV response with good reproducibility was obtained three successive times. When a 25.5-mm channel was used as a regressor, the lower signal was not accurately obtained (AR values were 0.13 and 0.21 under conditions 1 and 2,

(a) 37.5, 5.5 mm (b) 37.5, 13.5 mm (c) 37.5, 25.5 mm

(d) 25.5, 5.5 mm (e) 25.5, 13.5 mm

(f) 13.5, 5.5 mm

— Subtraction with short-distance regression
-- Lower-layer change (target)

Fig. 8 Subtraction result with short-distance regression of ΔOD measured while both layers are driven in condition 1, and ΔOD measured at a long distance while only lower layer (target) is driven. Combination of S-D distances: (a) 37.5 and 5.5 mm, (b) 37.5 and 13.5 mm, (c) 37.5 and 25.5 mm, (d) 25.5 and 5.5 mm, (e) 25.5 and 13.5 mm, and (f) 13.5 and 5.5 mm.

respectively) because this channel contained a considerable amount of the lower signal ($R_{\Delta OD} = 2.5$). In the phantom measurement, up to now, it has been difficult to change the absorption coefficient (or subsequent optical density) with complete reproducibility because conventional dynamic phantoms are based on a two-state control. Our dynamic phantom, in contrast, can be applied to a variety of signal discrimination methods.

5.4 Signal Discrimination with ICA

ICA is a signal discrimination method that extracts independent components from multiple signals without knowledge of the obtained signal by utilizing the statistical independence of the source components.[59] This method is effective for analyzing

(a) S-D: 5.5 mm (b) S-D: 13.5 mm

(c) S-D: 25.5 mm (d) S-D: 37.5 mm

Fig. 7 ΔOD measured at each S-D distance as upper and lower layers driven in white-noise and CBV waveform, respectively (condition 1). S-D distances: (a) 5.5 mm, (b) 13.5 mm, (c) 25.5 mm, and (d) 37.5 mm.
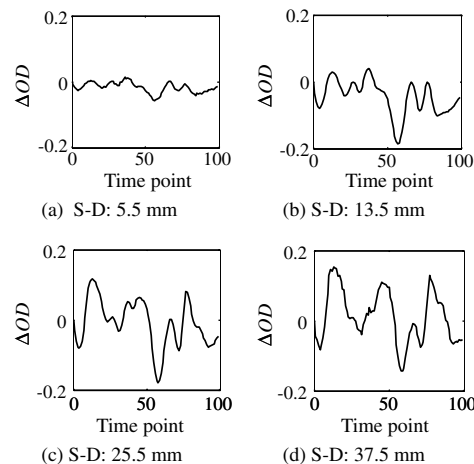

(a) S-D: 5.5 mm (b) S-D: 13.5 mm

(c) S-D: 25.5 mm (d) S-D: 37.5 mm

Fig. 9 ΔOD measured at each S-D distance as upper and lower layers were driven in waveform of biological fluctuation and CBV, respectively (condition 2). S-D distances: (a) 5.5 mm, (b) 13.5 mm, (c) 25.5 mm, and (d) 37.5 mm.

Fig. 10 Subtraction result with short-distance regression of ΔOD measured while both layers were driven in condition 2, and ΔOD measured at a long distance while only lower layer (target) was driven. Combination of S-D distances: (a) 37.5 and 5.5 mm, (b) 37.5 and 13.5 mm, (c) 37.5 and 25.5 mm, (d) 25.5 and 5.5 mm, (e) 25.5 and 13.5 mm, and (f) 13.5 and 5.5 mm.
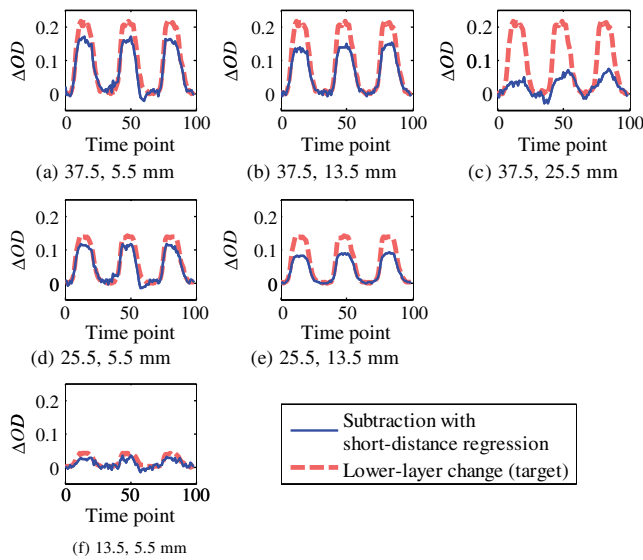
signals that have multiple signal sources and need to be measured at multiple points.[27,28]

ICA can be used to extract multiple independent components and weights at each measurement position. Original data can be reconstructed by totaling the products of independent components and weights. In this study, we used the time-delayed decorrelation (TDD)-ICA algorithm, which assumes that the time-delayed cross-correlation between independent components can vanish at any time.[28,60–62] Multiple signals used in this analysis are, in this case, the time series recorded at multiple S-D distances.

We tested whether or not we could discriminate between absorption changes of the upper and lower layers from the obtained ΔOD time course data with ICA when the absorption of both layers of the phantom were simultaneously changed (condition 2, stated above). The obtained components were compared with the ΔOD time-course data obtained when the absorption of only one layer was driven (actual signals). Performance was quantitatively evaluated on the basis of the correlation coefficient between the obtained component and the actual signal.

5.5 Results of Performance Evaluation of ICA Method

Using the data obtained under condition 2 (both layers driven; upper layer: biological fluctuation, lower layer: CBV), ICA was used to extract independent components and their weights at each S-D distance. Figure 11(a) plots the time course of

Table 1 Performance of subtraction method in extraction of lower-layer signal. Amplitude ratio (AR) of subtraction result to only lower-layer change (target) under three conditions: (a) AR from computed ΔOD; (b) experimental AR under condition 1; and (c) experimental AR under condition 2.

(a) AR from computed ΔOD

		Shorter S-D distance		
		5.5 mm	13.5 mm	25.5 mm
Longer S-D distance	37.5 mm	0.94	0.83	0.53
	25.5 mm	0.88	0.65	
	13.5 mm	0.65		

(b) Experimental AR under condition 1

		Shorter S-D distance		
		5.5 mm	13.5 mm	25.5 mm
Longer S-D distance	37.5 mm	0.77	0.59	0.13
	25.5 mm	0.86	0.56	
	13.5 mm	0.75		

(c) Experimental AR under condition 2

		Shorter S-D distance		
		5.5 mm	13.5 mm	25.5 mm
Longer S-D distance	37.5 mm	0.77	0.66	0.21
	25.5 mm	0.81	0.61	
	13.5 mm	0.62		
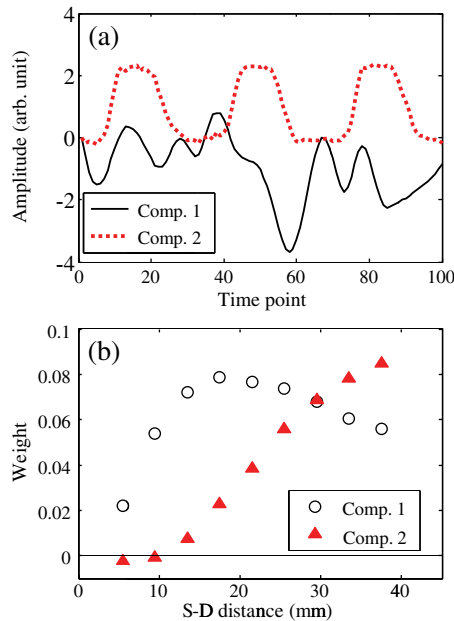
Fig. 11 ICA results. (a) Independent components extracted with ICA and (b) weights for each component at each S-D distance.

independent components extracted with ICA and Fig. 11(b) plots weights of each component at each S-D distance. The top-two largest components in the contributing ratio were extracted. Components 1 and 2 correspond to the absorption change of the lower and upper layers, respectively. The correlation coefficients between the independent components (extracted when both layers were driven) and the ΔOD time course (obtained at a 25.5-mm S-D distance in advance while only each layer was driven) were 0.988 (upper layer) and 0.996 (lower layer). (The channel of the 41.5-mm S-D distance was not used because of a low signal-to-noise ratio.)

The dependence of a component's weight on S-D distance was similar to that of ΔOD and L_{eff} (see Fig. 5). The reasons for the slight difference between these dependences are 1. the interference of one layer absorption change to the sensitivity to that of other layer's absorption change, 2. the correlation between two-layer waveforms, and 3. the measurement noise.

According to Eq. (2), ΔOD is the product of the change in absorption coefficient and partial effective path length, and therefore the weights at each S-D distance in Fig. 11(b) reflect the changes in partial effective path length depending on the S-D distance shown in Fig. 5. This result shows that the phantom simulates the absorption change in the entire layer by sliding the position of the absorber (the coefficient of which is fixed).

The effectiveness of ICA for discriminating between surface- and deep-layer effects was experimentally demonstrated under a condition in which the time-course changes in the absorption of the upper and lower layers were different (preferably, statistically independent). Such validation is difficult to ensure with human measurement because the exact amount of absorption change cannot be precisely known.

6 Concluding Remarks

6.1 Summary

We developed a dynamic phantom for simulating tissue with two absorption layers that are independently driven with two

one-axis automatic stages that can cause the absorption change of any waveform. When several simulated NIRS signals—such as white noise, physiological fluctuation, and CBV response—were created by the driving stages, the time-course data of ΔOD were obtained with a good reproducibility and linear relationship to stage-position changes. These results show that ΔOD (i.e., $\Delta\mu_a$) is caused by the stage-position change (Δx).

We used this phantom to evaluate the performance of a subtraction method with a short-distance regressor. When a short S-D distance channel that is not sensitive to lower-layer absorption change is used as a regressor, the signal that resulted from subtraction was in better agreement with the actual lower signal. Furthermore, to demonstrate the advantage of simulating absorption coefficient waveforms with our phantom, we applied an ICA method to the signals obtained while two layers were concurrently driven with different time courses. When the extracted components were compared to the signal obtained when the absorber of each layer was singly driven, the correlation coefficients were over 0.98 for both layers.

These results demonstrate that our dynamic phantom can be used to evaluate methods for discriminating between the effects of scalp and cerebral blood flow in NIRS signals.

6.2 Future Work

It has been reported that systemic fluctuations related to blood pressure or heart rate—in particular, because of dynamic cerebral autoregulation[63,64] or veins on the brain surface[34]—can influence the NIRS signal.[65,66] In these cases, to extract cerebral blood including systemic signal, we need to use a signal discrimination method that considers the dependence of signal amplitude on S-D distance instead of just the waveform characteristics of the signal. The dynamic phantom we developed in the present study should contribute to a direct validation of other methods to extract desired signals (e.g., a CBV signal) from mixed signals. It should be noted that, however, the results from this phantom cannot be easily generalized because the structure and optical properties of it are not the same as human. If this phantom model is extended to more realistic geometries with less spatial homogeneity, the result from the phantom would be more reliable and would contribute to the signal discrimination. In particular, the effects of correlation or covariance, frequency characteristics, and waveforms on signal-processing methods can be directly and quantitatively investigated.

References

1. F. F. Jöbsis, "Noninvasive, infrared monitoring of cerebral and myocardial oxygen sufficiency and circulatory parameters," *Science* **198**(4323), 1264–1267 (1977).
2. B. Chance et al., "Cognition-activated low-frequency modulation of light absorption in human brain," *Proc. Natl. Acad. Sci. U. S. A.* **90**(8), 3770–3774 (1993).
3. Y. Hoshi and M. Tamura, "Detection of dynamic changes in cerebral oxygenation coupled to neuronal function during mental work in man," *Neurosci. Lett.* **150**(1), 5–8 (1993).
4. A. Villringer et al., "Near infrared spectroscopy (NIRS): a new tool to study hemodynamic changes during activation of brain function in human adults," *Neurosci. Lett.* **154**(1–2), 101–104 (1993).

5. A. Maki et al., "Spatial and temporal analysis of human motor activity using noninvasive NIR topography," *Med. Phys.* **22**(12), 1997–2005 (1995).
6. Y. Yamashita, A. Maki, and H. Koizumi, "Near-infrared topographic measurement system: imaging of absorbers localized in a scattering medium," *Rev. Sci. Instrum.* **67**(3), 730–732 (1996).
7. H. Koizumi et al., "Higher-order brain function analysis by trans-cranial dynamic near-infrared spectroscopy imaging" *J. Biomed. Opt.* **4**(4), 403–413 (1999).
8. H. Koizumi et al., "Optical topography: practical problems and new applications," *Appl. Opt.* **42**(16), 3054–3062 (2003).
9. H. Sato, T. Takeuchi, and K. L. Sakai, "Temporal cortex activation during speech recognition: an optical topography study," *Cognition* **73**(3), B55–B66 (1999).
10. G. Taga et al., "Spontaneous oscillation of oxy- and deoxy-hemoglobin changes with a phase difference throughout the occipital cortex of newborn infants observed using non-invasive optical topography," *Neurosci. Lett.* **282**(1–2), 101–104 (2000).
11. F. Homae et al., "Development of global cortical networks in early infancy," *J. Neurosci.* **30**(14), 4877–4882 (2010).
12. E. Watanabe et al., "Noninvasive assessment of language dominance with near-infrared spectroscopic mapping," *Neurosci. Lett.* **256**(1), 49–52 (1998).
13. T. Suto et al., "Multichannel near-infrared spectroscopy in depression and schizophrenia: cognitive brain activation study," *Biol. Psychiatry* **55**(5), 501–511 (2004).
14. Y. Ito et al., "Assessment of heating effects in skin during continuous wave near infrared spectroscopy," *J. Biomed. Opt.* **5**(4), 383–390 (2000).
15. M. Kiguchi et al., "Comparison of light intensity on the brain surface due to laser exposure during optical topography and solar irradiation," *J. Biomed. Opt.* **12**(6), 062108 (2007).
16. H. Atsumori et al., "Development of wearable optical topography system for mapping the prefrontal cortex activation," *Rev. Sci. Instrum.* **80**(4), 043704 (2009).
17. H. Atsumori et al., "Noninvasive imaging of prefrontal activation during attention-demanding tasks performed while walking using a wearable optical topography system," *J. Biomed. Opt.* **15**(4), 046002 (2010).
18. T. Funane et al., "Synchronous activity of two people's prefrontal cortices during a cooperative task measured by simultaneous near-infrared spectroscopy," *J. Biomed. Opt.* **16**(7), 077011 (2011).
19. P. Smielewski et al., "Clinical evaluation of near-infrared spectroscopy for testing cerebrovascular reactivity in patients with carotid artery disease," *Stroke* **28**(2), 331–338 (1997).
20. T. J. Germon et al., "Sensitivity of near infrared spectroscopy to cerebral and extra-cerebral oxygenation changes is determined by emitter-detector separation," *J. Clin. Monit. Comput.* **14**(5), 353–360 (1998).
21. S. Kohri et al., "Quantitative evaluation of the relative contribution ratio of cerebral tissue to near-infrared signals in the adult human head: a preliminary study," *Physiol. Meas.* **23**(2), 301–312 (2002).
22. T. Takahashi et al., "Influence of skin blood flow on near-infrared spectroscopy signals measured on the forehead during a verbal fluency task," *NeuroImage* **57**(3), 991–1002 (2011).
23. E. Okada and D. T. Delpy, "Near-infrared light propagation in an adult head model: II. Effect of superficial tissue thickness on the sensitivity of the near-infrared spectroscopy signal," *Appl. Opt.* **42**(16), 2915–2922 (2003).
24. Y. Hoshi et al., "Reevaluation of near-infrared light propagation in the adult human head: implications for functional near-infrared spectroscopy," *J. Biomed. Opt.* **10**(6), 064032 (2005).
25. Y. Zhang et al., "Eigenvector-based spatial filtering for reduction of physiological interference in diffuse optical imaging," *J. Biomed. Opt.* **10**(1), 011014 (2005).
26. J. Virtanen, T. Noponen, and P. Merilainen, "Comparison of principal and independent component analysis in removing extracerebral interference from near-infrared spectroscopy signals," *J. Biomed. Opt.* **14**(5), 054032 (2009).
27. S. Kohno et al., "Removal of the skin blood flow artifact in functional near-infrared spectroscopic imaging data through independent component analysis," *J. Biomed. Opt.* **12**(6), 062111 (2007).
28. T. Katura et al., "Extracting task-related activation components from optical topography measurement using independent components analysis," *J. Biomed. Opt.* **13**(5), 054008 (2008).
29. V. Toronov et al., "Study of local cerebral hemodynamics by frequency-domain near-infrared spectroscopy and correlation with simultaneously acquired functional magnetic resonance imaging," *Opt. Express* **9**(8), 417–427 (2001).
30. R. Saager and A. Berger, "Measurement of layer-like hemodynamic trends in scalp and cortex: implications for physiological baseline suppression in functional near-infrared spectroscopy," *J. Biomed. Opt.* **13**(3), 034017 (2008).
31. R. B. Saager, N. L. Telleri, and A. J. Berger, "Two-detector Corrected Near Infrared Spectroscopy (C-NIRS) detects hemodynamic activation responses more robustly than single-detector NIRS," *NeuroImage* **55**(4), 1679–1685 (2011).
32. T. Yamada, S. Umeyama, and K. Matsuda, "Multidistance probe arrangement to eliminate artifacts in functional near-infrared spectroscopy," *J. Biomed. Opt.* **14**(6), 064034 (2009).
33. S. Umeyama and T. Yamada, "Monte Carlo study of global interference cancellation by multidistance measurement of near-infrared spectroscopy," *J. Biomed. Opt.* **14**(6), 064025 (2009).
34. Y. Tong, L. M. Hocke, and B.d Frederick, "Isolating the sources of widespread physiological fluctuations in functional near-infrared spectroscopy signals," *J. Biomed. Opt.* **16**(10), 106005 (2011).
35. Q. Zhang, E. N. Brown, and G. E. Strangman, "Adaptive filtering for global interference cancellation and real-time recovery of evoked brain activity: a Monte Carlo simulation study," *J. Biomed. Opt.* **12**(4), 044014 (2007).
36. Q. Zhang, G. E. Strangman, and G. Ganis, "Adaptive filtering to reduce global interference in noninvasive NIRS measures of brain activation: How well and when does it work?," *NeuroImage* **45**(3), 788–794 (2009).
37. Y. Zhang, J. Sun, and P. Rolfe, "Reduction of global interference in functional multidistance near-infrared spectroscopy using empirical mode decomposition and recursive least squares: a Monte Carlo study," *J. Europ. Opt. Soc. Rap. Public.* **6**, 11033 (2011).
38. L. Gagnon et al., "Improved recovery of the hemodynamic response in diffuse optical imaging using short optode separations and state-space modeling," *NeuroImage* **56**(3), 1362–1371 (2011).
39. B. W. Pogue and M. S. Patterson, "Review of tissue simulating phantoms for optical spectroscopy, imaging and dosimetry," *J. Biomed. Opt.* **11**(4), 041102 (2006).
40. M. Firbank and D. T. Delpy, "A design for a stable and reproducible phantom for use in near infrared imaging and spectroscopy," *Phys. Med. Biol.* **38**(6), 847 (1993).
41. C. D. Kurth et al., "A dynamic phantom brain model for near-infrared spectroscopy," *Phys. Med. Biol.* **40**(12), 2079–2092 (1995).
42. R. Lohwasser and G. Soelkner, "Experimental and theoretical laser-Doppler frequency spectra of a tissuelike model of a human head with capillaries," *Appl. Opt.* **38**(10), 2128–2137 (1999).
43. J. G. Kim and H. Liu, "Investigation of biphasic tumor oxygen dynamics induced by hyperoxic gas intervention: the dynamic phantom approach," *Appl. Opt.* **47**(2), 242–252 (2008).
44. P. H. Koh, C. E. Elwell, and D. T. Delpy, "Development of a dynamic test phantom for optical topography," *Adv. Exp. Med. Biol.* **645**, 141–146 (2009).
45. T. Funane et al., "Optical scanning system for light-absorption measurement of deep biological tissue," *Rev. Sci. Instrum.* **82**(9), 093101 (2011).
46. Y. Fukui, Y. Ajichi, and E. Okada, "Monte Carlo prediction of near-infrared light propagation in realistic adult and neonatal head models," *Appl. Opt.* **42**(16), 2881–2887 (2003).
47. S. Wang et al., "Effects of spatial variation of skull and cerebrospinal fluid layers on optical mapping of brain activities," *Opt. Rev.* **17**(4), 410–420 (2010).
48. M. Firbank, M. Oda, and D. T. Delpy, "An improved design for a stable and reproducible phantom material for use in near-infrared spectroscopy and imaging," *Phys. Med. Biol.* **40**(5), 955–961 (1995).
49. E. Okada and D. T. Delpy, "Near-infrared light propagation in an adult head model: I. Modeling of low-level scattering in the cerebrospinal fluid layer," *Appl. Opt.* **42**(16), 2906–2914 (2003).
50. F. B. Haeussinger et al., "Simulation of near-infrared light absorption considering individual head and prefrontal cortex anatomy: implications for optical neuroimaging," *PLoS One* **6**(10), e26377 (2011).
51. T. Funane et al., "Noncontact brain activity measurement system based on near-infrared spectroscopy," *Appl. Phys. Lett.* **96**(12), 123701 (2010).

52. T. Funane et al., "Noncontact optical brain activity measurement system using phosphor placed on skin," *Jpn. J. Appl. Phys.* **50**(7), 077001 (2011).

53. P. van der Zee and D. T. Delpy, "Simulation of the point spread function for light in tissue by a Monte Carlo Method," *Adv. Exp. Med. Biol.* **215**, 179–191 (1987).

54. M. Hiraoka et al., "A Monte Carlo investigation of optical pathlength in inhomogeneous tissue and its application to near-infrared spectroscopy," *Phys. Med. Biol.* **38**(12), 1859–1876 (1993).

55. E. Okada et al., "Theoretical and experimental investigation of near-infrared light propagation in a model of the adult head," *Appl. Opt.* **36**(1), 21–31 (1997).

56. R. B. Buxton et al., "Modeling the hemodynamic response to brain activation," *NeuroImage* **23**(Suppl. 1), S220–S233 (2004).

57. V. Toronov et al., "Near-infrared study of fluctuations in cerebral hemodynamics during rest and motor stimulation: temporal analysis and spatial mapping," *Med. Phys.* **27**(4), 801–815 (2000).

58. M. D. Fox et al., "Intrinsic fluctuations within cortical systems account for intertrial variability in human behavior," *Neuron* **56**(1), 171–184 (2007).

59. J. F. Cardoso, "Blind signal separation: statistical principles," *Proc. IEEE* **86**(10), 2009–2025 (1998).

60. L. Molgedey and H. G. Schuster, "Separation of a mixture of independent signals using time delayed correlations," *Phys. Rev. Lett.* **72**(23), 3634–3637 (1994).

61. A. Ziehe and K. Muller, "TDSEP—an efficient algorithm for blind separation using time structure," in *Proc. of ICANN 98*, 675–680, Springer Verlag, Berlin (1998).

62. R. Hirosaka et al., "Noisy time-delayed decorrelation and its application to extraction of neural activity from single optical recordings in guinea pigs," *Phys. D: Nonlinear Phenomena* **194**(3–4), 320–332 (2004).

63. R. Zhang et al., "Transfer function analysis of dynamic cerebral autoregulation in humans," *Am. J. Physiol. Heart Circ. Physiol.* **274**(1), H233–H241 (1998).

64. R. B. Panerai et al., "Dynamic cerebral autoregulation during brain activation paradigms," *Am. J. Physiol. Heart Circ. Physiol.* **289**(3), H1202–1208 (2005).

65. I. Tachtsidis et al., "Measurement of frontal lobe functional activation and related systemic effects: a near-infrared spectroscopy investigation," *Adv. Exp. Med. Biol.* **614**, 397–403 (2008).

66. I. Tachtsidis et al., "False positives in functional near-infrared topography," *Adv. Exp. Med. Biol.* **645**, 307–314 (2009).